Microfluid Nanofluid (2017) 21:17
DOI 10.1007/s10404-017-1853-3

RESEARCH PAPER

Transient flow of gravity-driven viscous films over 3D patterned substrates: conditions leading to Wenzel, Cassie and intermediate states

G. Karapetsas[1] · N. K. Lampropoulos[1] · Y. Dimakopoulos[1] · J. Tsamopoulos[1]

Received: 26 September 2016 / Accepted: 11 January 2017

Abstract We examine the transient film flow under the action of gravity over solid substrates with three-dimensional topographical features. Our focus is placed on the coating of a periodic array of rectangular cuboid trenches. The Navier–Stokes equations are solved using the volume-of-fluid method, fully taking into account the flow in both the liquid and gas phases. Using this scheme, we are able to determine the different wetting patterns that may arise depending on parameters such as the various geometrical characteristics of the trench, the lateral distance between them, the substrate wettability and the liquid viscosity. We present flow maps that describe the conditions under which the liquid film may successfully coat the patterned substrate, resulting in the so-called Wenzel state, or air may become entrapped inside the topography of the substrate. In the latter case, we describe in detail the position and shape of the air inclusions, how they are formed and the conditions under which coating can approach the ideal Cassie–Baxter state. We investigate in detail the effect of the sidewalls, typically ignored when considering the case of ideal 2D trenches (i.e., trenches extending to infinity in the lateral direction), through the enhancement of the viscous resistance inside the trench and the effect of capillarity in the case of narrow trenches. We also examine the coating behavior for a wide range of liquids and show that successful coating is favored for liquids with moderate viscosities. Finally, we perform simulations for the coating of two successive trenches in the flow direction and show that in the case of 3D trenches, the differences between the coating of the first and subsequent trenches are not significant.

Keywords Thin-film flow · Flow over topography · Coating flows · Air entrapment · Cassie and Wenzel states

1 Introduction

Film flows which are driven by a body force (such as gravity or centrifugal force) or even by the motion of the substrate itself can be encountered in various engineering applications such as spin coating (Stillwagon and Larson 1990), gravure printing (Yin and Kumar 2006; Grau et al. 2016) or flows in two-phase heat exchangers and adsorption or distillation columns using structured packings (Argyriadi et al. 2006). In practice, however, the surfaces encountered are never completely flat since they may contain well defined features in the form of sharp steps, trenches, pillars, corrugations, etc., while irregularities may also arise due to the presence of arrested drops and particles on the substrate. Besides thickness variations of the coated layer, the presence of these topographical features may also lead to air entrapment inside them under certain conditions, e.g., for very deep trenches or trenches with enhanced hydrophobicity, which, in turn, may affect significantly the flow dynamics as well as the resulting coating quality of the solid surface.

The flow of a liquid film over topographical features has drawn the attention of many researchers over the years; an informative review of the literature can be found in

Electronic supplementary material The online version of this article (doi:10.1007/s10404-017-1853-3) contains supplementary material, which is available to authorized users.

✉ J. Tsamopoulos
tsamo@chemeng.upatras.gr

[1] Laboratory of Fluid Mechanics and Rheology, Department of Chemical Engineering, University of Patras, 26500 Patras, Greece

Published online: 02 February 2017

Lampropoulos et al. (2016). The most studied case is the one that corresponds to the desired arrangement in many coating applications where the liquid fully wets the solid structure; this wetting state is also known as the Wenzel state. A number of theoretical (e.g., see Kalliadasis et al. 2000; Mazouchi and Homsy 2001; Gaskell et al. 2004; Bontozoglou and Serifi 2008; Lenz and Kumar 2007; Zhou and Kumar 2012) as well as experimental works (e.g., see Decré and Baret 2003 and Argyriadi et al. 2006) have demonstrated that the presence of topographical features leads to thickness variations of the coated layer due to the effect of the capillary and inertia forces. However, as it was mentioned above, a fully wetting state cannot always be achieved and in many cases air may become entrapped inside the topographical features, i.e., during the filling process. This often poses significant problems when for example it is desired to coat a uniform photoresist layer on a wafer surface with high topography structures (Huang and Wang 2014) or during cell filling with ink in gravure printing (Grau et al. 2016). On the other hand, air entrapment can be highly desired in applications where drag reduction is required and one characteristic example is the flow over a superhydrophobic surface (Ou and Rothstein 2005). It is well known that the remarkable water repellent properties of these surfaces do not lie in their surface chemistry alone, but also in the micro- or nanoscale surface structure (Cotin-Bizonne et al. 2003; Quére 2005; Bhushan et al. 2009). The presence of gas pockets trapped inside these structures leads to limited contact between the liquid and the solid surface enhancing the mobility of the liquid; this wetting state is known as the Cassie–Baxter state. As a result, when liquid flows over such surfaces the apparent slip length may become significantly enhanced; see the informative review by Rothstein (2010).

Theoretical efforts to account for the presence of air in the microstructure have focused mainly on idealized situations where it is often assumed that the liquid–gas interface is perfectly flat and/or pinned at the edges of the microstructure, i.e., assuming an ideal Cassie–Baxter state (Busse et al. 2013; Park et al. 2013). Using this approach, factors such as the effect of the direction of flow with respect to structure topography has been investigated by examining grooves arranged either transversely or longitudinally to the flow (Davies et al. 2006; Maynes et al. 2007; Belyaev and Vinogradova 2010). Such idealized considerations, however, only reveal part of the story and in many cases may simply not be sufficient, e.g., due to the non-negligible effect of a curved liquid–gas interface or due to the partial penetration of the liquid in the microstructure; this is supported by both experimental observations (Tsai et al. 2009) and numerical studies (Gao and Feng 2009; Teo and Khoo 2010; Karapetsas et al. 2016). The shape of the meniscus over the trench can be significantly affected, e.g., by the absolute pressure in the microchannel (Dilip et al. 2015). Moreover, the meniscus stability as well as the longevity of the gas pockets was found by Byun et al. (2008) to be very sensitive, under the same flow conditions, to the various geometrical characteristics. It has also been suggested that the longevity of the gas pockets can be affected by possible gas dissolution in the liquid phase (Lv et al. 2014; Xiang et al. 2016).

Taking all these into consideration, a fundamental question that arises is how in the first place, the flowing liquid may entrap gas inside the topographical features forming either a fully non-wetted or a partially wetted state and under which conditions fully wetted states can be encountered. In order to address this problem, one would have to examine the transient flow of the liquid coating the substrate; this, of course, requires including the motion of the contact line. Following the work of Goodwin and Homsy (1991) and Mazouchi et al. (2004), who studied the gravity-driven viscous flow over a flat plane with a moving contact line, Gramlich et al. (2004) were the first to investigate the time-dependent 2D flow of a Newtonian film over orthogonal trenches. Using the boundary integral method, these authors were able to produce maps of the various coating patterns which were found to depend on the trench width and depth as well as the substrate wettability. Very recently, Lampropoulos et al. (2016) examined the same problem, albeit using the Volume-Of-Fluid (VOF) method which enabled the investigation of cases with more complex dynamics, such as film pinching and merging or liquid impact on the solid wall, while taking fully into account the effect of inertia. Their study extended significantly the work presented earlier by Gramlich et al. (2004), providing more detailed flow maps of the resulting coating arrangements.

Although the transient 2D simulations in the above studies provide useful insights for the coating process, it is important to note that they merely represent an ideal situation. In fact, the various topographical features in almost every application in reality have a three-dimensional structure, e.g., arrays of pillars, ridges, holes and trenches. It is reasonable to expect that the actual 3D pattern of the substrate may affect significantly the resulting flow and thus the coating process; an experimental study on the effect of texture of superhydrophobic surfaces on the amount and shape of the entrapped air can be found in Bodji et al. (2009). These authors, however, focused their study on the longevity of the bubbles after they have formed and did not examine the conditions and dynamics which lead to their entrapment. The latter is actually the goal of the present work which is carried out by examining in detail the transient 3D gravity-driven flow of a Newtonian film over a substrate with 3D structure. To this end, we typically consider the case of a film which encounters a periodic array of rectangular cuboid trenches. At this point, it would be

appropriate to make a comment regarding the so-called rivulet instability that may arise along the moving contact line of a thin film down an inclined plane (Huppert 1982). It has been established that this instability is related to the formation of a capillary ridge due to the effect of viscous forces, just behind the advancing contact line; a detailed review on these instabilities can be found in Craster and Matar (2009). Short wavelengths are stabilized by the effect of capillarity, while the cutoff wave number of the instability, above which all modes are stable, is approximately equal to 0.8 which corresponds to a dimensional wavelength $\lambda \approx 7.9$ l; where $l = h_N(3\mathrm{Ca})^{-1/3}$ is the well-known length scale associated with the capillary ridge and h_N is the Nusselt film thickness (e.g., see Troian et al. 1989; Spaid and Homsy 1996; Kondic and Diez 2001). For $\mathrm{Ca} = 0.1$, the cutoff wavelength is $l \sim 12h_N$, while for $\mathrm{Ca} = 0.015$ it increases to $l \sim 22h_N$. In all simulations that we will report in this paper, the repeated unit of the total width is well below this limit. Here, however, our focus is placed on the coating of a periodic array of trenches, the periodicity of which is typically shorter than the cutoff wavelength beyond which these spanwise modes become unstable. For the purposes of our study, and in order to reduce the computational cost, we will consider a physical domain which contains just a single spatial period (applying periodic boundary conditions in the spanwise direction), and thus, the emergence of such instabilities will not be encountered. Finally, for the purposes of our study, we will employ a similar methodology to Lampropoulos et al. (2016) using the VOF scheme and examine in detail the different wetting patterns depending on the dimensions of the topography, the capillary and Reynolds numbers and the wettability of the substrate.

This paper is organized as follows: in Sect. 2, the problem formulation along with the governing equations is given, and the numerical implementation is shortly discussed in Sect. 3. The discussion of the results from our numerical simulations along with flow maps in terms of the trench dimensions, the lateral distance between trenches, the different contact angles and the Kapitza number are presented in Sect. 4. In the end of this section, coating of multiple trenches even in the flow direction is examined. Conclusions are drawn in Sect. 5.

2 Problem formulation

We consider the 3D, gravity-driven, transient flow of a Newtonian, incompressible, liquid film over a solid, vertical substrate featuring a 3D rectangular cuboid trench (see Fig. 1a). At the inlet, the film is assumed to be fully developed with height, H_1, while at the front it forms a moving contact line with the solid substrate, where the value of the contact angle, θ, is imposed. This boundary condition is justified by the fact that the dynamic contact line is not expected to change much from the static advancing contact angle as long as the wetting line speed is slow, which corresponds to low values of the capillary number; the latter

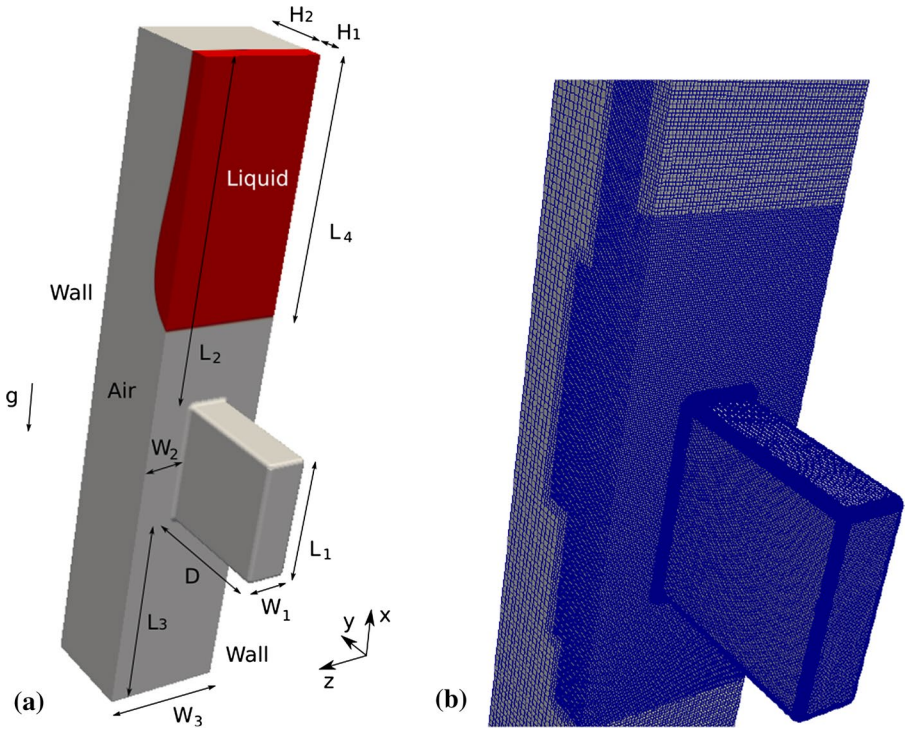

Fig. 1 **a** Schematic of a film flowing down a vertical substrate with a rectangular cuboid trench. **b** Typical mesh used for the simulations (for clarity we show only a region around the trench). In this and all subsequent figures, the camera has been placed behind the substrate wall and at an angle with *y*-axis (~43°), while the *vertical axis* of the image is shown tilted with respect to *x*-axis (~26°). Note that the exact distance of the camera from the substrate wall may vary depending on the desired field of view

condition applies for all the calculations that will be presented in this manuscript. We fully account for the presence of air which lies ahead and above the film. In order to reduce the computational needs of our simulations, we confine the air-occupied domain by a second vertical and straight wall, which is placed at a sufficient distance away from the film interface, H_2, in order not to affect appreciably the film velocity and shape. Both fluids present in the system are considered to be incompressible, viscous and immiscible. The density and viscosity, are, respectively, ρ_l and μ_l for the liquid and ρ_g and μ_g for the gas phase, while the surface tension of the liquid–gas interface, σ, is assumed to be constant. The liquid film flows steadily down the vertical substrate until it reaches the entrance of a rectangular cuboid trench of depth, D, width, W_1, and length, L_1. Depending on the flow conditions, the gravity-driven liquid film wets the inner surface of the trench either fully or partially; in the latter case, air inclusions may form inside the trench. We use a Cartesian coordinate system to model the dynamics with its x-axis opposite to the direction of the flow and parallel to the vertical wall, its y-axis normal to it and its z-axis in the lateral direction, centered at the exit boundary.

In the present work, we make use of the VOF method which provides a simple way of accounting for both the liquid and gas phases and treating even large topological changes of their interface. The numerical scheme that has been used in the present work is identical to the one in Lampropoulos et al. (2016), and therefore, we will not attempt to explain all the details here, but merely present in summary the key points of the method that we have used. In the VOF method, the motion of the interface between immiscible liquids of different density and viscosity is defined by a phase indicator, the volume fraction function in each computational cell, c, of the liquid phase which varies from 0 to 1. Thus, the interface lies in the transition region occupied by cells where $0 < c < 1$. Using the volume fraction function, c, it is possible to evaluate the averaged values of the density, ρ, and the viscosity, μ, employing the following expressions:

$$\rho = \rho_l c + \rho_g (1 - c), \quad \mu = \mu_l c + \mu_g (1 - c), \tag{1}$$

where the subscript l and g denote the property of the liquid and gas phase, respectively.

One of the critical issues of the VOF method is the boundedness and conservation of the volume fraction, c. This is especially the case in flows with high density and viscosity ratios, where small errors in volume fraction may lead to inaccurate calculations of physical properties and surface curvature. Various attempts have been made in order to overcome these difficulties (e.g., see Gopala and van Wachem 2008; Fraggedakis et al. 2015). Here, we use a method known as "interface compression" scheme proposed by Wardle and Weller (2013). According to this scheme, the mass conservation of each phase is imposed by solving the following transport equation for the volume fraction:

$$\partial_t c + \nabla \cdot (\boldsymbol{u} c) + \nabla \cdot (\boldsymbol{u}_r c(1 - c)) = 0, \tag{2}$$

where $\boldsymbol{u} = u_x \boldsymbol{e}_x + u_y \boldsymbol{e}_y + u_z \boldsymbol{e}_z$ denotes the velocity vector ($\boldsymbol{e}_i (i = x, y, z)$ are the Cartesian unit vectors) and $\boldsymbol{u}_r$ is an artificial "compression velocity" applied normally to the interface to compress the volume fraction field and maintain a sharp interface. The $c(1 - c)$ term ensures that this term is only active in the interface region, while the value for the artificial interface "compression velocity" is evaluated at the cell faces from the velocity magnitude at the interface region and it is given by $\boldsymbol{u}_r = |\boldsymbol{u}|\boldsymbol{n}$; here $\boldsymbol{n} = \nabla c / |\nabla c|$ denotes the unit vector normal to the liquid/air interface pointing outward from the liquid.

The flow is governed by the momentum and mass conservation equations

$$\rho(\partial_t \boldsymbol{u} + \boldsymbol{u} \cdot \nabla \boldsymbol{u}) + \nabla P - \nabla \cdot \left[\mu \left(\nabla \boldsymbol{u} + \nabla \boldsymbol{u}^T\right)\right] - \rho \boldsymbol{g} - \delta \sigma \kappa \boldsymbol{n} = 0, \quad \nabla \cdot \boldsymbol{u} = 0. \tag{3}$$

In the above equations, ∇ denotes the gradient operator in Cartesian coordinates, P is the pressure and $\boldsymbol{g} = -|g|\boldsymbol{e}_x$ is the gravitational acceleration. Surface tension effects are incorporated in the momentum balance by means of the continuum surface force (CSF) model formulated by Brackbill et al. (1992), and the terms $\kappa = -\nabla \cdot \boldsymbol{n}$ and δ in the momentum equation denote, respectively, the mean curvature of the interface and the Dirac delta function, which signifies that capillarity should be applied only locally at the liquid/air interface.

In terms of boundary conditions, the no-slip and no-penetration conditions are imposed on the solid walls and atmospheric conditions are imposed at the outlet. In order to reduce the computational cost, we solve for half of the domain shown in Fig. 1 and apply symmetry boundary conditions on the side boundaries. At the inlet of the domain, the location of the liquid/air interface, H_1, is imposed, along with a fully developed velocity profile of both phases between vertical walls. By neglecting the air viscosity with respect to that of the liquid, it is possible to derive the following profiles for the x-component of the velocity field which is imposed as a boundary condition at the inlet

$$u_{x,l} = \frac{\rho_l - \rho_g}{2\mu_l} g H_1^2 \left(2\frac{y}{H_1} - \frac{y^2}{H_1^2}\right),$$
$$u_{x,g} = \frac{\rho_g - \rho_l}{2\mu_l} g \frac{H_1}{H_2} \left[y H_1 - (H_1 + H_2) H_1\right]. \tag{4}$$

Moreover, at the dynamic contact line we impose a constant contact angle, θ. To initiate the simulation, we introduce the

steady solution that we get from the corresponding 2D simulation for a flat substrate (see Lampropoulos et al. 2016) and place the contact line at a distance $L_i = L_2 - L_4 \simeq 4H_1$ from the entrance of the trench.

3 Implementation of the VOF method and grid generation

The implementation of the numerical algorithm described above has been done using the open source "OpenFOAM" (version 2.3.1) CFD software package, because of its versatility, accuracy and inherent capability to handle 3D flows. An important ingredient of the numerical algorithm is the generation of a good quality mesh in order to ensure the accuracy of the numerical solution. For the production of a typical mesh that is shown in Fig. 1b, the following steps are followed: (a) We employ a CAD software to generate the desired geometry of the physical domain in stereolithography (STL) format; (b) a background mesh is generated using the utility "blockMesh" and finally, (c) we use the automatic hex mesh utility "snappyHexMesh" to create a volume mesh around the StL object in 3D. The resulting mesh approximately conforms to the surface, and local refinement is applied where it is needed the most, i.e., 2 levels of refinement are applied around and inside the trench (at a distance at least $5H_1$ from each side) as well as around the position of the liquid/air interface, 4 levels of refinement are applied near the curved corners and 1 level of refinement is applied along the solid surface everywhere else (see Fig. 1b). We should note that in order to avoid the problems that can be encountered when considering geometrically sharp right angles, we followed a similar approach with Lampropoulos et al. (2016) and considered curved angles instead. A similar modification has been made by Gramlich et al. (2004) and Pavlidis et al. (2010, 2016) who reported that it did not affect their results appreciably. This was done here by creating 3D fillets on all the edges of the solid objects using the CAD software. The fillet radius was set to 0.2 H_1 which is much smaller than the typical trench dimensions that we have considered. To ensure that the flow is well resolved, we placed around and inside the trench at least 16 elements per film height in all directions. Numerical checks showed that increasing the number of elements further led to negligible changes.

Finally, we should note that we carried out several tests to determine the optimum values of L_2, L_3, H_2 that have been used for the simulations that will be presented below. These parameters were selected so that they do not affect film flow, especially around the trench. Accounting for the bulge at the front of the film, we found out that $H_2 = 4H_1$ for $\theta = 30°$ and $H_2 = 8H_1$ for $\theta \geq 60°$ is sufficient for the confined air thickness not to affect the film flow appreciably. The required entrance length should be in the range of $15H_1 \leq L_2 \leq 40H_1$, and this was determined by the steady shape of the film which was calculated from the 2D simulations (Lampropoulos et al. 2016). The exit length was set at $L_3 = 15H_1$. To ensure the code stability and accuracy, the integration in time was done using an automatically adjusted time step setting the maximum Courant number to 0.5. A typical grid that has been used for our simulations consists of 2×10^6 to 5×10^6 number of cells (these must be multiplied by 4 to get the corresponding number of unknowns) depending of the actual size of our physical domain. The parallel execution is implemented on a PC equipped with AMD Opteron 6376 CPU @ 2.30 GHz (32 cores), 192 GB RAM, using message passing interface (MPI) and computation time varied between 2 and 7 days. Part of the computations was also performed on "ARIS" National HPC Infrastructure of the Greek Research and Technology Network.

4 Results and discussion

The physical properties of the liquids and air that we have used in the simulations to be presented below are given in Table 1, while the corresponding values of the Kapitza number, $Ka = \sigma \rho_l^{1/3} \Big/ \left(g^{1/3} \mu_l^{4/3}\right)$ are given in Table 2. We considered liquids with different viscosities and surface tensions to model the cases of water or more viscous fluids such as dilute polymeric solutions often encountered in coating processes. Moreover, to cover a wide range of liquids we have also considered liquids with intermediate viscosity values. We should note that all calculations have been performed with dimensional quantities. Nonetheless, all the results to be presented below will be in

Table 1 Physical properties of the liquids we used ($g = 9.81$ m/s^2)

Material property (units)	Liquid 1 ($i = l$)	Liquid 2 ($i = l$)	Liquid 3 ($i = l$)	Liquid 4 ($i = l$)	Liquid 5 ($i = l$)	Liquid 6 ($i = l$)	Water ($i = l$)	Air ($i = g$)
μ_i (Pa s)	1	1	0.03	0.005	0.0025	0.0015	0.001	1.5×10^{-5}
ρ_i (kg/m^3)	10^3	10^3	10^3	10^3	10^3	10^3	10^3	1
σ (N/m)	0.03	0.07	0.07	0.07	0.07	0.07	0.07	–

Table 2 Dimensionless numbers and the resulting film thickness for the examined cases

Case	I	II	III	IV	V	VI	VII
Ka	0.14	0.33	35.08	382	964	1904	3270
Ca	0.1	0.015	0.015	0.015	0.015	0.015	0.015
Re	1.65×10^{-3}	3.43×10^{-4}	0.382	13.7	54.9	153	343
Liquid (see Table 1)	1	2	3	4	5	6	Water
H_1 (μm)	553	327	327	327	327	327	327

dimensionless form to facilitate the comparison of our work with previous studies in the literature. To this end, we scale all lengths with H_1, velocities with $\rho_l g H_1^2/\mu_l$, pressure with σ/H_1 and time with $\mu_l/\rho_l g H_1$. Inserting the above scalings into the governing equations, the dimensionless groups that arise are the capillary number $Ca = \rho_l g H_1^2/\sigma$ and the Reynolds number $Re = \rho_l^2 g H_1^3/\mu_l^2$. Given the chosen characteristic velocity, these dimensionless numbers have the same definition as the Bond and the Archimedes numbers, respectively. Table 2 also presents the values of *Ca* and *Re* for various cases that we have examined, which correspond to the reported dimensional film thicknesses, H_1. All lengths, presented thereafter, are normalized with this film height.

For the case of ideal 2D trenches, it has already been established (Lampropoulos et al. 2016) how the material, flow and geometric parameters may lead to the three possible configurations, i.e., (a) completely filled trench (Wenzel state), (b) partially filled trench with air inclusions and (c) total non-wetting state (Cassie–Baxter state). The objective of the present work is to go one step further and investigate the wetting characteristics of repeated rectangular cuboids forming a 3D pattern of trenches. To this end, we examine first in detail the effect of the various geometric characteristics on the resulting coating behavior for hydrophilic surfaces under creeping flow conditions and then proceed to investigate the effects of surface wettability and fluid inertia. We close our discussion by also examining the coating of a substrate with multiple trenches.

4.1 Code validation

Before we proceed with the presentation of our results, we would like to note that our numerical code has been validated and its predictions were thoroughly compared against the results presented by Lampropoulos et al. (2016). These authors use an identical numerical scheme to ours, albeit in 2D, and we were able to accurately reproduce their 2D simulations with our 3D code. Nevertheless, in order to increase further our confidence in the code that we have

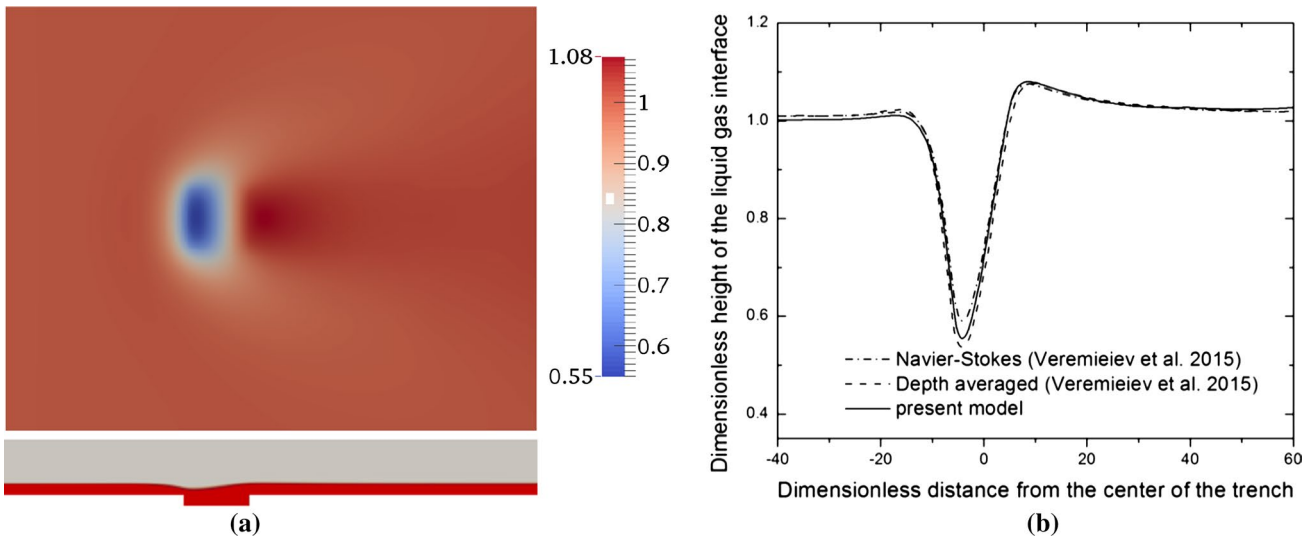

Fig. 2 **a** *Top panel* contour lines of the height of the upper liquid gas interface in the *x*–*z* plane; direction of the flow is from *left* to *right*. *Bottom panel* shape of the liquid–gas interface at the plane of symmetry ($z = 0$). **b** Height of the upper liquid gas interface along the centerline ($z = 0$) compared with the numerical solutions presented by Veremieiev et al. (2015) in their Fig. 15. The parameter values for our simulations are $Ca = 0.164$, $Re = 0.00012$, $D = H_1$, $L_1 = W_1 = 12H_1$, $W_2 = L_2 = L_3 = 100H_1$ and substrate inclination angle 7°. Only part of the domain is shown in this figure ($-40H_1 \le x \le 60H_1$,$-40H_1 \le z \le 40H_1$), while the center of trench is placed at $x = 0$ and $z = 0$. Here, flow is from *left* to *right*

developed, we also provide a comparison in Fig. 2 of the fully developed viscous flow over topography exhibiting a shallow square trench with $D = H_1$, $L_1 = W_1 = 12H_1$ at flow conditions resulting in $Ca = 0.164$, $Re = 0.00012$; the inclination angle of the substrate is 7° with respect to the horizontal. In order to ensure a fully developed profile, we consider a domain which is very long, i.e., $W_2 = L_2 = L_3 = 100H_1$; only part of the domain is shown in this figure ($-40H_1 \leq x \leq 60H_1$, $-40H_1 \leq z \leq 40H_1$), while the center of the trench is placed at $x = 0$ and $z = 0$. Figure 2a depicts contour lines of the dimensionless height of the liquid gas interface in the x–z plane which reveals the capillary depression, the downstream surge and the bow wave structure typical of such flows (Gaskell et al. 2004; Veremieiev et al. 2015). It should be noted that under creeping flow conditions, such as the case examined here, a downstream surge is not encountered in the ideal 2D flow, but as it was explained by Gaskell et al. (2004) its appearance can simply be attributed to the finite length and width of the trench. Fluid enters the trench in two different directions, streamwise (over the upstream wall) and spanwise (over the sidewalls), due to lateral pressure gradients resulting from the spanwise curvature of the interface. However, the only possible way to exit the trench is through the downstream wall, and since its width is shorter than the entrance the downstream surge arises to accommodate the flow. Veremieiev et al. (2015) examined this case (see their Fig. 15) and provided solutions employing both the exact solutions of the Navier–Stokes equation with a sharp interface model using the finite element method and a depth averaged model, under creeping flow conditions ($Re = 0$). These authors have considered the case of a steep trench, and thus, in order to make a meaningful comparison we considered for this case curved corners with fillet radius equal to 0.05 H_1. Figure 2b depicts the dimensionless height of the liquid–air interface along the centerline ($z = 0$), and as it is shown the agreement is very good. The small discrepancy in the prediction of the capillary depression could be attributed to some extend to the presence of a curved angle in our simulations since it is known to cause a slightly increased depression compared to the case of a steep trench (Veremieiev et al. 2015).

4.2 Effect of the geometrical characteristics of the trench

4.2.1 Typical patterns and flow map (Case I and $\theta = 30°$)

We begin our study by considering a hydrophilic surface with contact angle, $\theta = 30°$, and a liquid, the properties of which are described by Case I in Table 2; the 2D flow of a liquid with exactly the same properties has been examined in detail by Lampropoulos et al. (2016). In general, the process of film coating of a rectangular cuboid trench is comprised of the following phases: At first, the film descends the vertically positioned flat substrate with a constant velocity and a permanent ridge shape. As it was already noted in Sect. 1, for the purposes of this study we consider a physical domain the width of which is significantly smaller than the cutoff wavelength beyond which the flow becomes unstable to spanwise modes forming fluid fingers (Spaid and Homsy 1996). Therefore, during this phase the flow remains steady and two-dimensional, without the presence of any fingering instabilities. At some point, the film reaches the trench entrance where the contact line motion decelerates and the shape of the film ridge readjusts until the capillary forces that have been developed drive the liquid inside the trench. Animation of the film dynamics is given in the Supporting Information (Movies S1, S2, S3, S4, S5 and S6 which correspond to the cases shown in Figs. 3, 6, 7, 10, 12 and 18, respectively). The flow up to this point exhibits some similarities with that in Lampropoulos et al. (2016) although it is clear that in our case the film also has to adjust in the spanwise direction before entering the trench. When the liquid eventually enters the trench driven by capillarity, it advances along the inner upstream and side walls of the trench while the height of the capillary ridge gradually decreases as the liquid fills

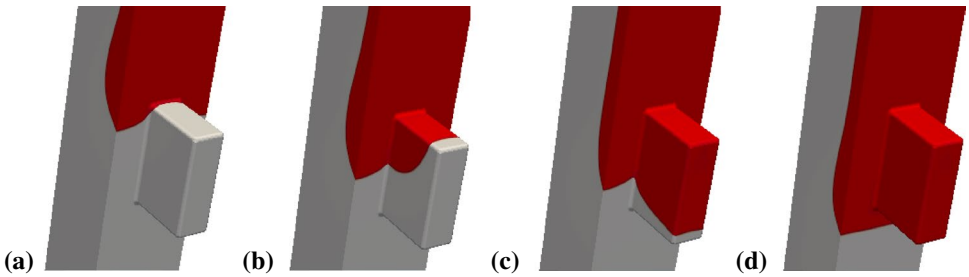

Fig. 3 (Case I) Development of a liquid film entering, completely filling and exiting the trench. The remaining parameters are $D = 4H_1$, $L_1 = 6H_1$ and $W_1 = W_2 = 2H_1$ and $\theta = 30°$. The corresponding times are **a** $t = 1.78$, **b** $t = 5.99$, **c** $t = 9.14$, **d** $t = 16.49$. An animation of the present simulation is given in the Supporting Information (Movie S1)

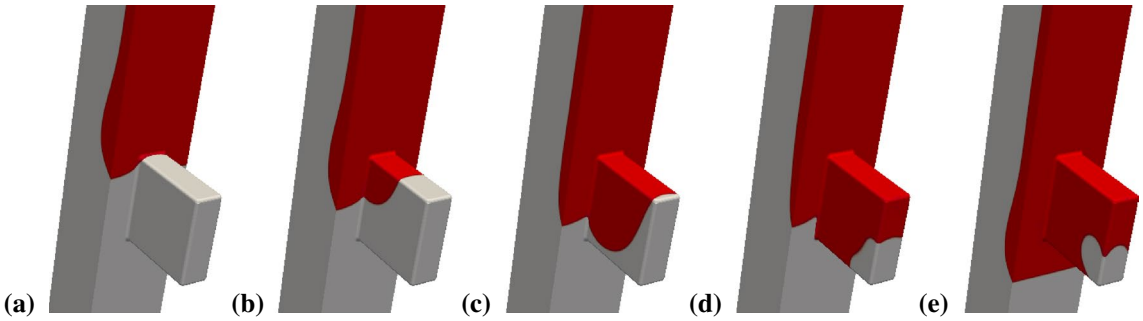

Fig. 4 (Case I) Development of a liquid film entering, partially filling and exiting the trench. The remaining parameters are $D = L_1 = 6H_1$, $W_1 = W_2 = 2H_1$ and $\theta = 30°$. The corresponding times are **a** $t = 1.78$, **b** $t = 5.99$, **c** $t = 10.19$, **d** $t = 12.29$, **e** $t = 20.69$

the trench. The advancing film front typically consists of a contact line along the flat vertical substrate next to the trench and the contact lines that are formed along the trench walls. As it will be shown below, depending on the size and shape of the cuboid trench and the lateral distance between the trenches, a variety of different configurations may be encountered.

The simplest possible configuration is the one shown in Fig. 3 for $D = 4H_1$, $L_1 = 6H_1$ and $W_1 = W_2 = 2H_1$; in this and all subsequent figures, time has been set to zero when the contact point has just reached the arc of the convex corner in the entrance (i.e., at a distance $0.2H_1$ from the upstream wall). In the case depicted in Fig. 3, when the liquid film reaches the trench entrance its motion decelerates whereas part of it tries to bypass the trench from the side. Eventually, the pressure gradient produced by the capillary force on the bulge of the film drives the film inside the trench, along both the upstream and side walls, overcoming the wall friction which resists wall wetting and the gravitational force which pulls the film downwards. The flow inside the trench has also to overcome the viscous resistance caused by the presence of the sidewalls in order to fully wet the trench. Due to the confinement that is caused by the sidewalls, the effect of capillarity also comes into play. Since in our case the substrate is hydrophilic, capillarity acts as to drive more liquid inside the trench while also helping its advancement in the downward direction; the opposite effect would be expected in the case of hydrophobic surfaces. The contact line along the upstream wall soon reaches the trench floor, advances along it and reaches first, before the contact line that advances along the sidewalls, the downstream wall. Once the trench gets filled with liquid, the capillary ridge of the film front takes form again and the liquid film continues to advance away from the trench. When the contact line is well beyond the trench, the free film surface above the trench assumes its well-known characteristics down a vertical plane, which includes the presence of a capillary rise and depression before the entrance and exit of the trench, respectively, and a downstream surge just after the trench, as shown in Fig. 2. Hereafter, we will refer to this arrangement as "Full Coating" (FC).

Another configuration is encountered for slightly deeper trenches, as shown in Fig. 4. Here, we consider a trench with $D = 6H_1$, while keeping the remaining dimensions the same with those in Fig. 3. The contact line in this case runs along the upstream trench wall and the sidewalls (Fig. 4a–c) when at some instant the liquid front defined by the contact lines along the sidewalls comes into contact with the downstream wall, before the contact line along the upstream wall reaches the trench bottom; this leads to air entrapment between the liquid and the bottom wall of the trench (Fig. 4d). We also observe that the liquid remains deeper in the edges of the cuboid due to the effect of capillary forces. It is well known that interior corners may enhance capillary effects by increasing the local curvature of the liquid surface in order to satisfy the contact angle wetting condition (see Higuera et al. 2008; Ponomarenko et al. 2011). Eventually the bubble acquires a steady shape and becomes entrapped in the downstream corner of the trench (Fig. 4e). A similar "Bubble in the Downstream Corner" (BDC) arrangement has been identified in the case of ideal 2D trenches by Lampropoulos et al. (2016). The main difference between their case and ours is the fact that the bubble in the 2D trench was infinitely long in the lateral direction, whereas in the 3D case it is confined by the presence of the sidewalls. As it is shown in Fig. 4e, the bubble in this case is in full contact with both sidewalls, the downstream wall and the trench floor. We will refer to this configuration as BDC_1. Depending on the size of the bubble that forms and the width of the trench, other configurations are also possible: (a) The bubble marginally reaches the sidewalls while the edges between the walls are wetted by the liquid (BDC_2) and (b) the bubble attaches only to the downstream wall and the trench floor in the mid-plane without contacting the sidewalls (BDC_3); such arrangements can be seen in Fig. 5.

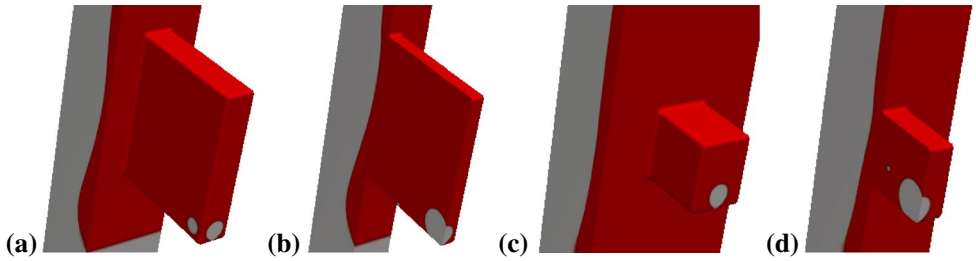

Fig. 5 (Case I) **a**, **b** Formation of bubble in the downstream corner marginally reaching the sidewalls (BDC_2): for $\theta = 30°$, $D = 8H_1$, $L_1 = 10H_1$, $W_1 = W_2 = 2H_1$ at $t = 45.27$. **c**, **d** Formation of bubble in the downstream corner not reaching the sidewalls (BDC_3): for $\theta = 30°$, $D = L_1 = 4H_1$, $W_1 = W_2 = 3H_1$ at $t = 20.06$. **a**, **c** Full view, **b**, **d** cut plane at the plane of symmetry

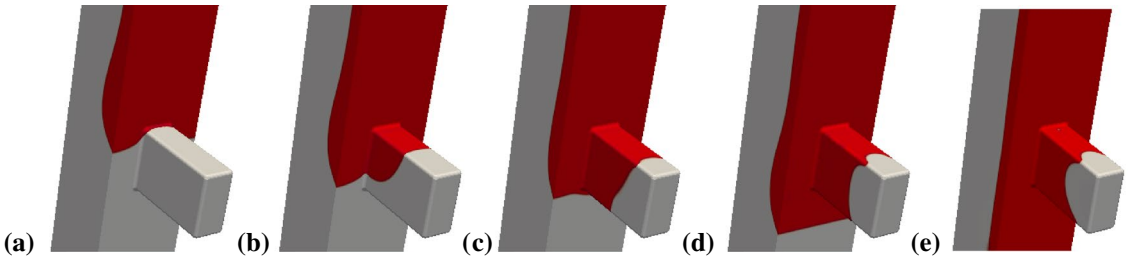

Fig. 6 (Case I) Development of a liquid film entering, partially filling and exiting the trench. The remaining parameters are $D = 6H_1$, $L_1 = 4H_1$ and $W_1 = W_2 = 2H_1$ and $\theta = 30°$. The corresponding times are **a** $t = 1.78$, **b** $t = 5.99$, **c** $t = 8.09$, **d** $t = 12.29$, **e** $t = 26.99$. An animation of the present simulation is given in the Supporting Information (Movie S2)

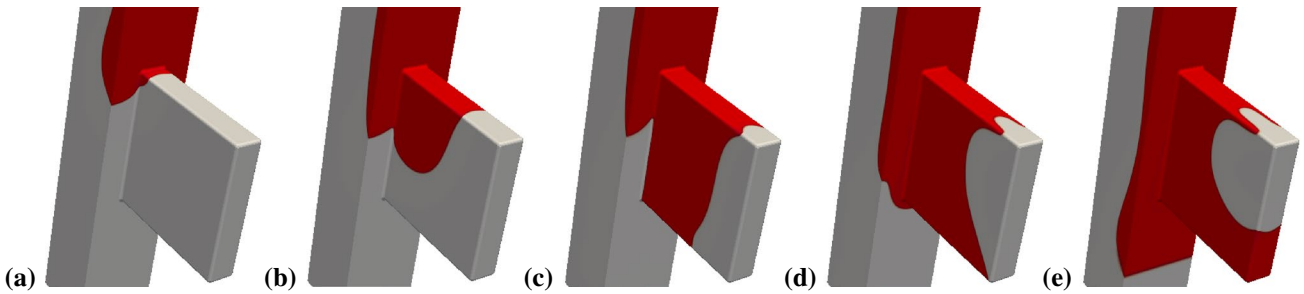

Fig. 7 (Case I) Development of a liquid film entering, partially filling and exiting the trench. The remaining parameters are $D = L_1 = 10H_1$, $W_1 = W_2 = 2H_1$ and $\theta = 30°$. The corresponding times are **a** $t = 3.26$, **b** $t = 11.66$, **c** $t = 24.26$, **d** $t = 32.67$, **e** $t = 41.07$. An animation of the present simulation is given in the Supporting Information (Movie S3)

When the trench has the same depth as in Fig. 4 but is not long enough (see Fig. 6 where the case with $L_1 = 4H_1$ is shown), the film front first encounters the downstream wall while the contact line along the upstream wall has not managed yet to reach the trench floor (see Fig. 6c). This leaves entrapped air in the entire bottom of the trench forming a separate liquid/air interface. When the liquid front touches the downstream wall, the spreading of the contact line along it takes place very fast, due to the large difference between the dynamic and the equilibrium contact angle. At the same time, fluid is also drawn there due to the effect of gravity from the upper part of the trench, and these two effects lead to partial dewetting of the upstream wall (see Fig. 6d). Eventually the inner liquid/air interface acquires a steady shape as the liquid film advances away from the trench (see Fig. 6e). This arrangement has been called "Capping Failure" (CF) in the literature (Gramlich et al. 2004; Lampropoulos et al. 2016).

On the other hand, for very long and sufficiently deep trenches, such as the case shown in Fig. 7 for $D = L_1 = 10H_1$ (the remaining parameters are the same with Fig. 3), another possibility arises. When the liquid front reaches the downstream wall (see Fig. 7c), the contact line has already penetrated inside the trench to such

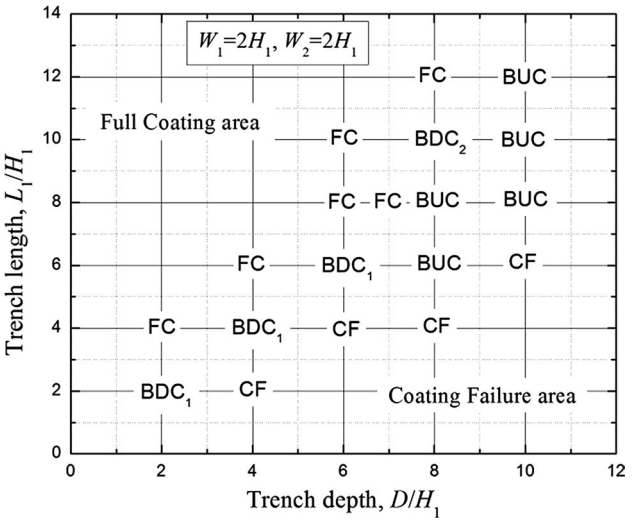

Fig. 8 Flow map with possible liquid arrangements depending on the trench depth, D, and length, L_1. The remaining parameters are $W_1 = W_2 = 2H_1$ and $\theta = 30°$ (Case I)

an extent that during the readjustment phase, after the air entrapment takes place, the contact line along the downstream wall reaches the trench floor (see Fig. 7d). Subsequently, the advancement of the contact line along the trench floor in the upstream direction leads to enhanced dewetting of the upstream wall before eventually the bubble acquires a steady shape. The resulting arrangement resembles the "Bubble in the Upstream Corner" (BUC) described in Lampropoulos et al. (2016), and we will use the same nomenclature hereafter.

A more complete picture of the possible configurations that can be encountered is given in Fig. 8, where we plot a flow map varying the length, L_1, and depth, D, of the cuboid trench while keeping fixed its width, $W_1 = 2H_1$, and the lateral distance between the trenches, $W_2 = 2H_1$; we performed simulations for $2H_1 \leq D \leq 10H_1$ and $2H_1 \leq L_1 \leq 12H_1$. In all cases presented in this figure, the simulation has approached a steady state inside the trench and the advancing contact line is well downstream the trench exit. In line with the 2D results presented by Gramlich et al. (2004) and Lampropoulos et al. (2016), we find that for a given trench depth, D, there is a critical minimum trench length, L_{1c}, required for achieving full coating (FC) of the trench; the full coating area appears in the top left corner of the map while partial coating or total coating failure corresponds to the bottom right part of the map. With increasing trench depth, D, the critical minimum length, L_{1c}, increases considerably. This is because the deeper the trench, the time required by the contact line along the upstream wall to reach the trench floor, and subsequently the downstream wall, increases. A similar behavior was also described by Lampropoulos et al. (2016) for an ideal 2D trench. In their case, however, the critical length was found to reach a plateau for depths larger than $5H_1$ (and smaller than the run out length) which is not seen here. The penetration of the liquid along the upstream wall takes place due to the surface tension effects and contact line dynamics. However, due to the additional viscous resistance caused by the presence of the sidewalls, the motion of the contact line along the upstream wall decelerates, making it more difficult to compete with the liquid that advances along the vertical direction under the effect of gravity.

We also observe in Fig. 8 that the BUC arrangement is encountered for trenches less deep than their 2D counterparts. It was shown in Lampropoulos et al. (2016) that such an arrangement can be found for trenches deeper than the so-called "run out length." The run out length has been defined in Gramlich et al. (2004) and Lampropoulos et al. (2016) as the maximum depth of a 2D trench up to which the upstream wall of the trench can be fully coated, and it has been predicted to be approximately equal to $11.8H_1$, for the present parameter values. The fact that BUC configuration arises for depths significantly smaller than this value is a clear indication that the run out length in the case of 3D trenches is affected by the additional viscous resistance due to the presence of the sidewalls. Indeed, by considering a trench which is deep enough, in order to avoid any interaction of the liquid film with the trench floor, the run out length has been evaluated, for the specific values of W_1 and W_2, to be approximately equal to $8.6H_1$; the effect of the trench width on the run out length will be examined in detail below.

For trenches with depth smaller than the estimated run out length, a narrow regime arises between the capping failure and the full coating regime, which corresponds to the BDC$_1$ configuration described in Fig. 4, similarly to the 2D case. When the depth is slightly smaller than the run out length between the two limiting arrangements (CF and FC), the BUC regime also arises followed by a BDC pattern for longer trenches. For trenches deeper than the run out length, as it was already mentioned, full coating cannot be achieved and the BUC configuration is encountered for long enough trenches.

Lampropoulos et al. (2016) have also shown that for very long trenches the film bulge may become very extended developing a thin neck which eventually pinches off leading to a continuous dripping of the film. To examine whether this behavior is encountered in our case, we have considered the trench shown in Fig. 9, where the dripping failure would be expected for the corresponding 2D case, i.e., for trench with the same depth and length. Nonetheless, as it is shown in this figure, instead of dripping failure we get the formation of a bubble in the upstream corner (BUC). This happens because the sidewalls provide

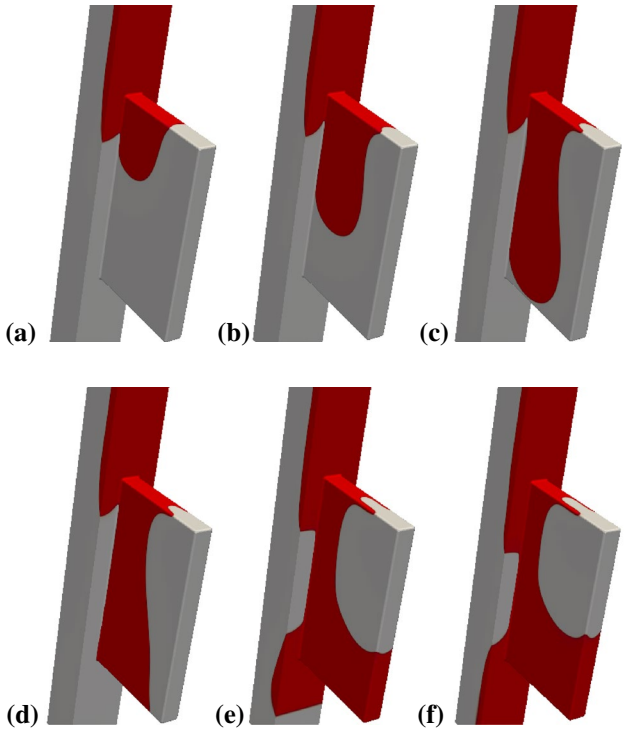

Fig. 9 (Case I) Development of a liquid film entering, partially filling and exiting the trench. The remaining parameters are $D = 12H_1$, $L_1 = 21H_1$, $W_1 = W_2 = 2H_1$ and $\theta = 30°$. The corresponding times are **a** $t = 15.86$, **b** $t = 32.67$, **c** $t = 49.47$, **d** $t = 53.68$, **e** $t = 70.48$ and **f** $t = 99.89$

support for the liquid–gas interface not allowing for the neck to become sufficiently thin for it to become unstable. Thus, the advancing front of the bulge is allowed to reach the downstream wall without the existence of any dripping. Moreover, here the trench is much longer than that in Fig. 7 and hydrophilicity along with capillarity act for a longer time, promoting the faster advancement of the liquid front inside the trench before reaching the downstream wall than along the flat vertical substrate next to the trench. This ultimately leads to the temporary appearance of a dry spot outside the trench (see Fig. 9e), which eventually becomes wetted at later times.

4.2.2 *Effect of trench width and lateral distance between trenches (Case I and $\theta = 30°$)*

So far, it has become clear that the finite width of the trench may affect significantly the coating process. For example, the simulations presented in Figs. 4, 5 and 6 (for $W_1 = W_2 = 2H_1$) predict partial coating of the trench, and this behavior is markedly different from the case of an ideal 2D trench (infinite width W_1) with exactly the same depth, D, and length, L_1, where full coating of the trench is predicted (Lampropoulos et al. 2016). The differences should obviously be attributed to the 3D characteristics of the flow which are mainly affected by two factors: (a) the finite trench width and (b) the lateral distances between the trenches.

A characteristic example of how these factors may affect the dynamics, and the resulting arrangement of the coated film is presented in Fig. 10. In this figure, we present the liquid film dynamics for a trench with $D = L_1 = W_1 = 4H_1$ and $W_2 = 3H_1$. The increased lateral distance between the trenches allows the film to advance faster along the flat part of the substrate, next to the trench, the edge of which normal to the flow decelerates it while the dynamic contact angle readjusts to approach 30° now with the upstream trench wall (Lampropoulos et al. 2016). This allows the film to eventually surpass the cavity by the time liquid starts to enter inside the trench (see Fig. 10a, b). The trench gets filled both from the side and the upstream walls while the liquid moves faster along the edges due to the enhanced effect of capillarity in these regions; note that in contrast to the previous cases the effect of sidewalls here is not as significant due to the larger width of the trench. At some

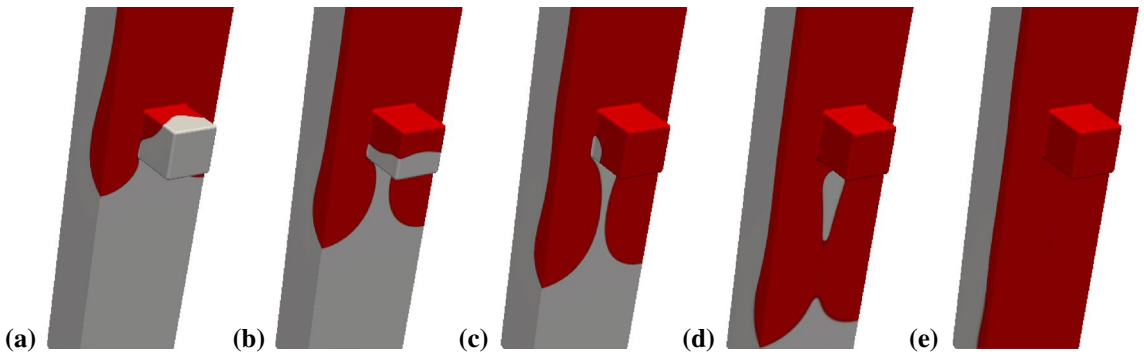

Fig. 10 (Case I) Development of a liquid film entering, filling and exiting the trench (Case I). $D = L_1 = 4H_1$, $W_1 = 4H_1$, $W_2 = 3H_1$ and $\theta = 30°$. The corresponding times are **a** $t = 7.44$, **b** $t = 11.66$, **c** $t = 15.86$, **d** $t = 24.26$ and **e** $t = 32.67$. An animation of the present simulation is given in the Supporting Information (Movie S4)

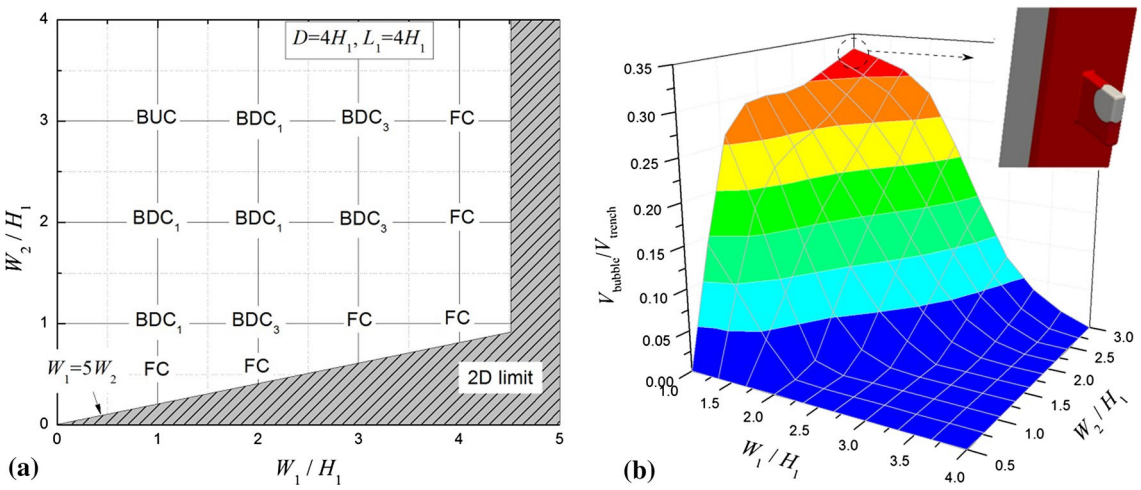

Fig. 11 (Case I) **a** Flow map with possible liquid arrangements depending on the trench width, W_1 and lateral distance between the trenches, W_2, and **b** corresponding bubble volume fraction ($V_{\text{bubble}}/V_{\text{trench}}$) inside the trench. The remaining parameters are $D = L_1 = 4H_1$ and $\theta = 30°$

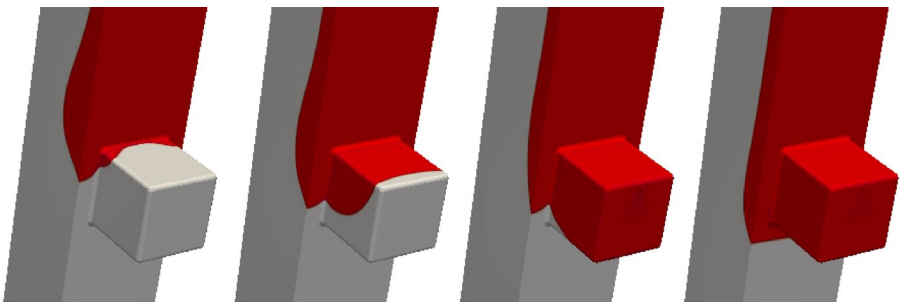

Fig. 12 (Case I) Development of a liquid film entering, filling and exiting the trench. $D = L_1 = 4H_1$, $W_1 = 4H_1$, $W_2 = H_1$ and $\theta = 30°$. The corresponding times are **a** $t = 3.89$, **b** $t = 8.09$, **c** $t = 10.19$ and **d** $t = 16.49$. An animation of the present simulation is given in the Supporting Information (Movie S5)

point, the liquid film rejoins ahead of it and forms a dry spot (see Fig. 10c, d) while the trench becomes completely coated; eventually the dry spot also becomes wetted by the liquid film (see Fig. 10e).

In order to examine the effect of these two factors in more detail, we consider a trench with depth $D = L_1 = 4H_1$ and vary the width, W_1, and lateral distance, W_2. We performed simulations for $H_1 \leq W_1 \leq 4H_1$ and $0.5H_1 \leq W_2 \leq 3H_1$ and plotted a flow map of the resulting configurations in Fig. 11a. As expected, varying the width, W_1, and lateral distance, W_2 of the trench leads to very different coating behaviors. As it was mentioned above, we already know that for the corresponding 2D case, i.e., for an ideal 2D trench with same D and L_1, full coating is predicted (Lampropoulos et al. 2016). In principle, it should be possible to recover the 2D limit when the following criteria are met: (a) $W_1 \gg H_1$ or (b) $W_1 \gg W_2$; these limiting conditions are satisfied in the grayed area of the flow map, and indeed full coating is predicted in this limiting regime as in the ideal 2D case. The first condition ($W_1 \gg H_1$) implies that when the width of the trench is much larger than the film height, from the liquid side the trench would appear as one with infinite length and the liquid film away from the sidewalls would not feel their presence and thus the solution should resemble the case of an ideal 2D trench with infinite width. On the other hand, assuming that we have many identical trenches next to each other and their width is much larger than the distance between them ($W_1 \gg W_2$), the flow between the trenches would become insignificant and the flow would have to go necessarily through the trenches; such an example is presented in Fig. 12.

As we move away from the 2D limit (toward the upper left corner in Fig. 11a), air entrapment becomes more pronounced. This is shown clearly in Fig. 11b where we have evaluated the ratio of the volume of the entrapped bubble with respect to the volume of the trench and plot it as a function of W_1 and W_2. The volume ratio of the entrapped bubble increases considerably for $W_1 = H_1$ and $W_2 = 3H_1$, which corresponds to a relatively narrow trench and leads to the formation of a bubble in the upstream corner; the inset in Fig. 11b shows the long time profile of the entrapped bubble for this case.

In the discussion of Fig. 7, it was mentioned that the run out length for $W_1 = W_2 = 2H_1$ was found to be significantly smaller than for the case of an ideal 2D trench. In order to examine in more detail the effect of sidewalls

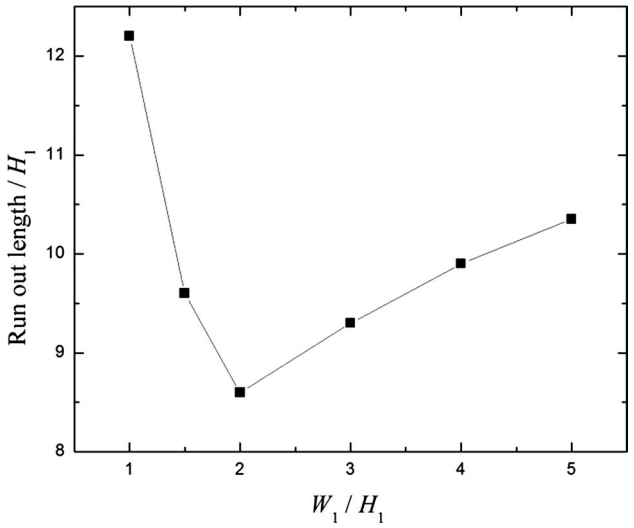

Fig. 13 (Case I) Dependence of the run out length on the trench width, W_1. The remaining parameters are $W_2 = 2H_1$ and $\theta = 30°$

on the run out length, we have evaluated it for trenches with varying widths and depict the results in Fig. 13. As it is shown in this figure, the run out length depends non-monotonically on the width of the trench. For very wide trenches, the run out length approaches the 2D limit which corresponds to trenches with infinite width. Clearly, the additional viscous resistance caused by the presence of the sidewalls renders the run out length for a 3D trench smaller with decreasing trench width, W_1. However, for hydrophilic surfaces such as the ones under study in this section, the effect of capillarity becomes increasingly important in the case of narrow trenches, which leads to a sharp increase of the run out length for very small values of W_1.

4.3 Effect of substrate wettability (Case I)

We proceed in our study with the examination of the effect of the substrate wettability. To this end, we consider trenches with same width and lateral distance between them as in Fig. 8; we also retain the same liquid, the properties of which are described by Case I in Table 2. We performed calculations for substrates with decreasing hydrophilicity, i.e., $\theta = 60°$ and 90°, and present the corresponding flow maps in Fig. 14. When examined in conjunction with Fig. 8, it can be clearly seen that with increasing values of θ, the regime for which full coating of the trench can be achieved decreases significantly. This is in line with the predictions for a 2D trench and, as explained in Lampropoulos et al. (2016), it can be attributed to the fact that decreasing hydrophilicity of the substrate leads to considerable decrease of the run out length. The capillary forces in the contact line region along the upstream wall are not strong enough to draw the liquid in the horizontal direction, and thus, the film front moves preferentially downwards under the effect of gravity. Moreover, when comparing the flow maps in Fig. 14 with the corresponding maps for an ideal 2D trench, it becomes evident that partial coating is favored in 3D trenches also in the case of less hydrophilic surfaces.

We should also note that for $\theta = 60°$, an additional flow pattern arises for $D = 4H_1$ and $L_1 = 6H_1$. In this case, a bubble forms in the downstream wall of the trench without coming into contact with sidewalls (see Fig. 15b which

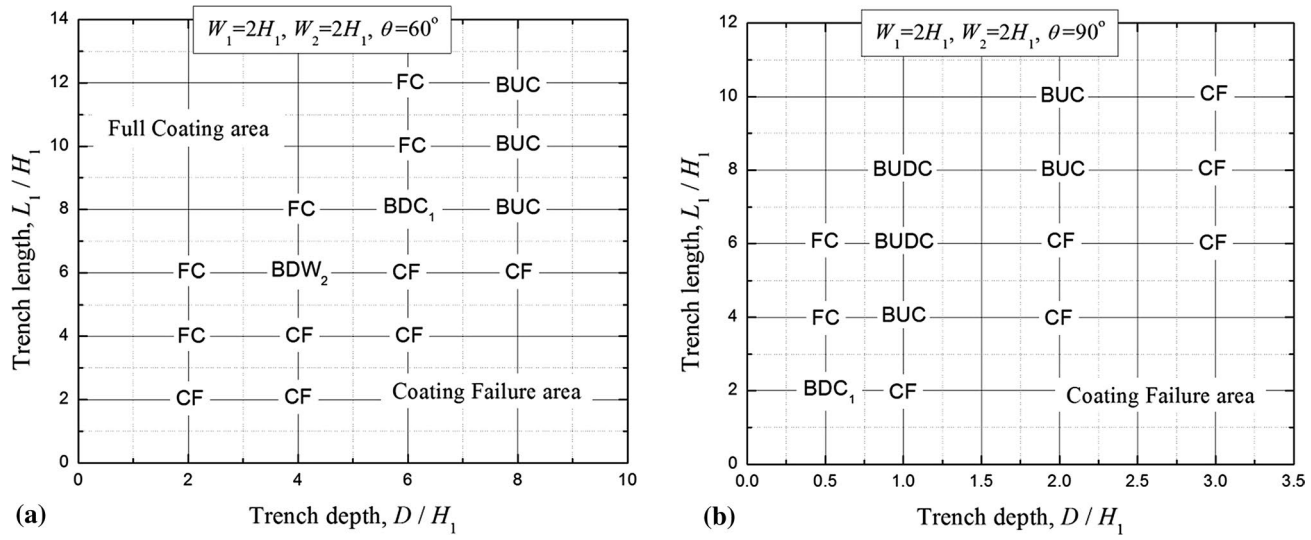

Fig. 14 (Case I) Flow maps with possible liquid arrangements depending on D and L_1 for **a** $\theta = 60°$ and **b** $\theta = 90°$. The remaining parameters are $W_1 = W_2 = 2H_1$

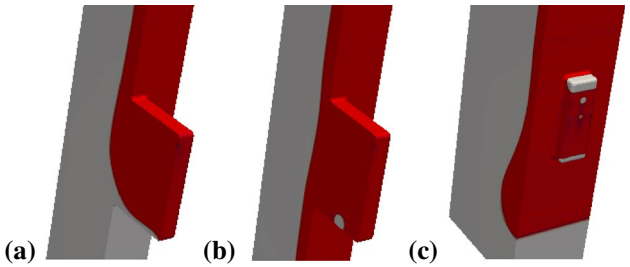

Fig. 15 (Case I) Formation of bubble in the downstream wall not reaching the sidewalls (BDW_2): for $\theta = 60°$, $D = 4H_1$ and $L_1 = 6H_1$ at **a** $t = 10.88$ and **b** $t = 30.78$; cut plane at plane of symmetry. **c** Formation of bubble in the upstream and downstream corner (BUDC): for $\theta = 90°$, $D = H_1$ and $L_1 = 6H_1$ at $t = 15.76$. The remaining parameters are $W_1 = W_2 = 2H_1$

shows a cut plane at the plane of symmetry); we will refer to this arrangement as BDW_2. This arrangement is possible when the contact line along the trench floor reaches the downstream wall almost simultaneously with the liquid front inside the trench (see Fig. 15a). Depending on the size of the bubble that forms and the width of the trench a similar configuration where the bubble reaches the sidewalls is also possible, we will refer to this configuration as (BDW_1). Lampropoulos et al. (2016) also noted that for $\theta = 90°$ another configuration is possible, where bubbles form both in the upstream and downstream corners. As it can be seen in Fig. 14b, this arrangement is also possible in the case of a cuboid trench; the resulting coating is also depicted in Fig. 15c.

In order to examine the effect of the trench sidewalls for surfaces with different wettability, we produced the flow map shown in Fig. 16a where we vary the contact angle, θ, and the trench width, W_1, while keeping fixed the remaining geometric characteristics of the trench ($D = L_1 = 4H_1$ and $W_2 = H_1$). As it is shown in this figure, in the case of a hydrophobic substrate ($\theta = 90°$), the liquid film fails to wet the trench even for wide trenches and the regime where the "Capping Failure" arises widens significantly. The ratio of the volume of the entrapped air over the trench volume is presented in Fig. 16b. The percentage of the entrapped air increases monotonically with the contact angle, while for the hydrophobic substrate ($\theta = 90°$) the trench is almost entirely filled with air approaching the ideal Cassie–Baxter state, especially for the smaller W_1.

In realistic applications, it is often difficult to see through the liquid to detect objects buried beneath the film or to examine the quality of the resulting coating. Since it is known that the presence of substrate topography leads to a disturbance in the surface of the coated film, it has been suggested that, in principle, it could be possible to recover this information by looking at the topography of the coated film (e.g., see Hayes et al. 2000; Heining and Aksel 2009; Rawlings et al. 2015); it has been noted, though, that the presence of flow could complicate things significantly, e.g., by causing an upstream shift to the film topography. One question that arises in our case is whether it would be possible to identify the coating configuration and presence of bubbles inside the trench by simply looking at the height of the liquid–gas interface from the top. To see whether this could be possible, we depict in Fig. 17 contour plots of the interfacial height for two very different configurations which arise for a hydrophilic (Fig. 17a) and a hydrophobic substrate (Fig. 17b); the bottom panels depict the liquid film at the plane of symmetry. In the former case, the BDC_1 pattern arises whereas in the latter case almost the entire trench is filled with air. As expected, we find that a capillary depression arises as the liquid flows above the trench,

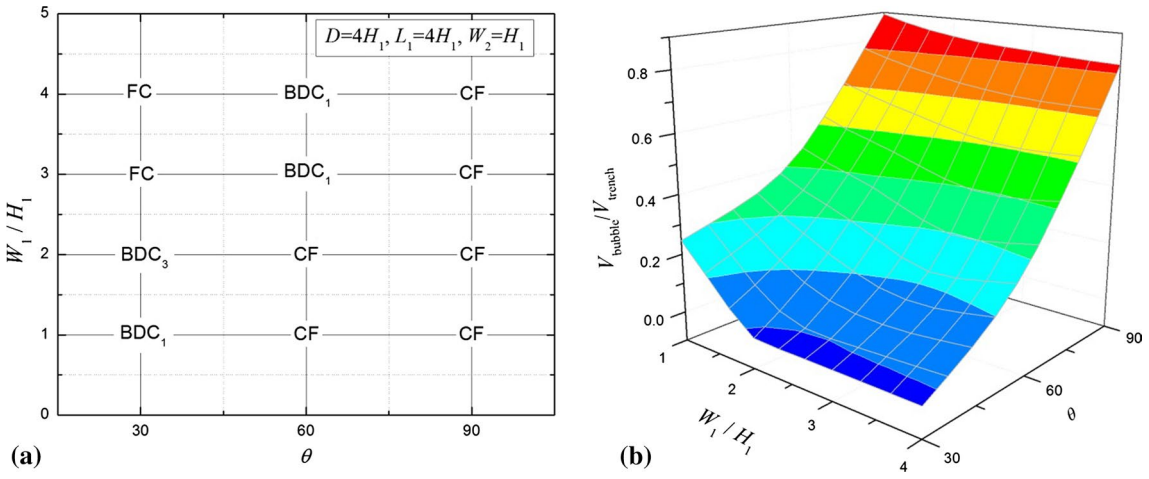

Fig. 16 (Case I) **a** Flow maps with possible liquid arrangements depending on W_1 and θ. **b** Bubble volume fraction inside the trench as a function of W_1 and θ. The remaining parameters are $D = L_1 = 4H_1$ and $W_2 = H_1$

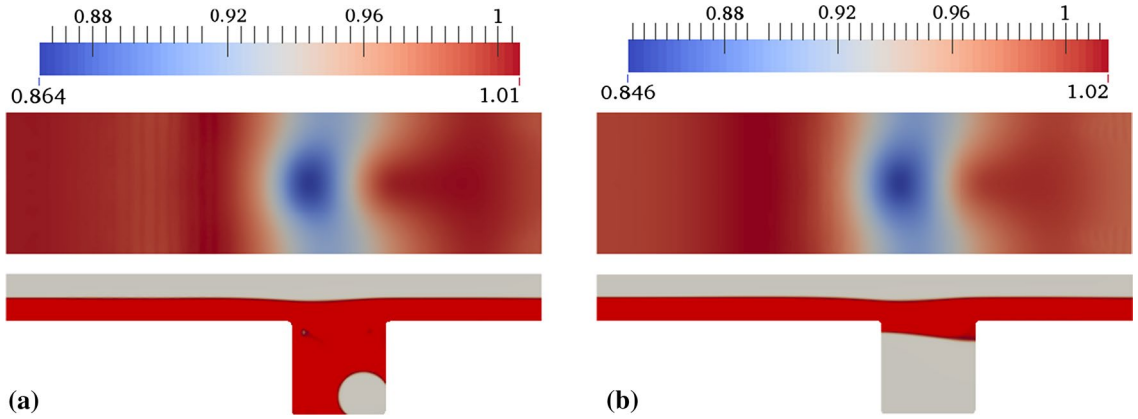

Fig. 17 (Case I) *Top panels* depict contour lines of the height of the upper liquid gas interface in the x–z plane. *Bottom panels* depict the shapes of both liquid–gas interfaces at the plane of symmetry. The remaining parameters are $D = L_1 = 4H_1$, $W_1 = W_2 = 2H_1$ and **a** $\theta = 30°$ and **b** $\theta = 90°$. Here, the flow is from *left* to *right*

which resemble the patterns found by Gaskell et al. (2004) and Veremieiev et al. (2015) in the case of fully coated trenches (see also Fig. 2 above). Interestingly, despite the large difference in the resulting arrangement of the film and the volume and shape of the entrapped air, the depth of the capillary depression is only slightly affected, i.e., less than 2%. We also note that for the hydrophilic surface the capillary depression is slightly reduced in comparison with the hydrophobic case, although the liquid that enters inside the trench has to cover larger distance before exiting from it. It appears, though, that the increased capillary pressure due to the presence of the bubble in the downstream corner and the highly curved interface acts cooperatively with the depression of the upper liquid–gas interface. On the other hand, this mechanism does not play a role in Fig. 17b where the bottom interface is almost flat.

4.4 Effect of Kapitza number

In this part of our study, we investigate the effect of the Kapitza number. This dimensionless number does not depend on the flow conditions but is solely a function of the liquid properties. In practice, the Kapitza number varies mainly due to the liquid viscosity since for most common liquids the variation for surface tension and density is not very large. Therefore, the variation of Ka here is accomplished by examining liquids with different viscosities, while keeping the rest of the properties constant. To this end, we consider liquids 2–6 as well as the case of water (see Table 1). In addition, we keep the value of the capillary number fixed and equal to $Ca = 0.015$, and thus, the cases that will be examined correspond to Cases II–VII in Table 2.

In Table 3, we present a flow map for a trench with depth $D = L_1 = 4H_1$, $W_2 = 2H_1$ and $\theta = 60°$. This flow map has been created by examining the different coating patterns that may arise for various values of the Ka number by considering trenches with different widths, W_1. Interestingly, the resulting coating patterns of the substrate are found to depend strongly on the value of Ka and in fact exhibit a non-monotonic dependence. The lowest value of Ka that we have used (i.e., $Ka = 0.33$) corresponds to the case of the most viscous fluid. The value of Re in this case is very small (see Table 2), and thus, the effect of inertia is negligible whereas the capillary forces become dominant driving the liquid inside the trench. However, due to the presence of the sidewalls, viscous resistance (which is enhanced due to the high viscosity of the liquid) slows down the motion of the liquid along the upstream wall while the liquid influx pushes the liquid in the vertical direction. This leads to partial filling of the trench and eventually, for all values of W_1, a bubble arises in the downstream corner. For moderate values of Ka, the viscous resistance becomes less important allowing for the liquid to penetrate faster

Table 3 (Case VII) Flow maps with possible liquid arrangements depending on the value of Ka and trench width W_1 for the case of water and $\theta = 60°$

	$W_1 = H_1$	$W_1 = 2\,H_1$	$W_1 = 3\,H_1$	$W_1 = 4\,H_1$
$Ka = 0.33$ (Case II)	BDC_1	BDC_3	BDC_3	BDC_1
$Ka = 35.1$ (Case III)	BDW_1	BDW_2	FC	BDW_2
$Ka = 382$ (Case IV)	FC	FC	FC	FC
$Ka = 964$ (Case V)	FC	FC	FC	FC
$Ka = 1904$ (Case VI)	BDW_1	BDC_1	BDC_1	BDC_1
$Ka = 3270$ (Case VII)	BDC_1	CF	CF	CF

The remaining parameters are $D = L_1 = 4H_1$ and $W_2 = 2H_1$

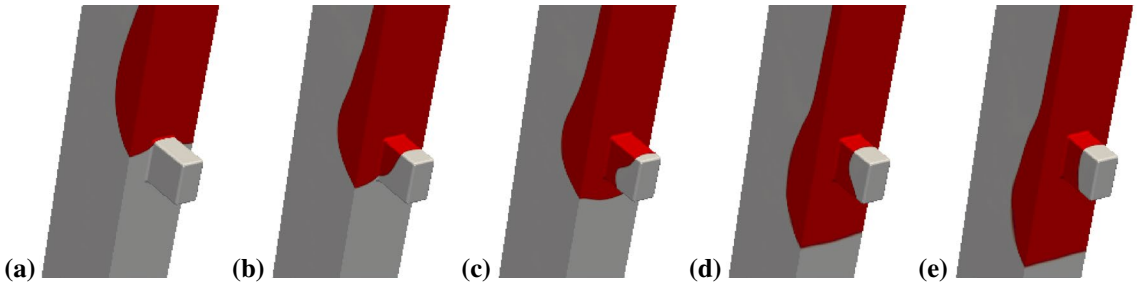

Fig. 18 (Case VII) Development of a liquid film entering, partially filling and exiting the trench. The corresponding times are **a** $t = 3.21$, **b** $t = 16.05$, **c** $t = 22.47$ and **d** $t = 41.72$. The remaining parameters are $D = L_1 = 4H_1$, $W_1 = W_2 = 2H_1$ and $\theta = 60°$. An animation of the present simulation is given in the Supporting Information (Movie S6)

along the upstream wall and to fully coat the trench. Increasing further the value of *Ka* inertia starts to play a significant role and helps the liquid to overcome the constant capillary force (*Ca* is kept constant), which acts in the horizontal direction. Thus, for the two highest values of *Ka* we find that the trench is only partially coated while in the case of water (Case VII) large part of the trench is occupied by gas, resulting in capping failure (CF); the evolution of the film dynamics for water are shown in Fig. 18.

The poor ability of water to coat surfaces which are either mildly hydrophilic (e.g., $\theta = 60°$) or hydrophobic $\theta = 90°$ was also noted by Lampropoulos et al. (2016) in the case of ideal 2D trenches. These authors, however, did not attempt to produce any flow maps for such substrates and focused mostly their attention on the remarkable ability of water to wet very deep trenches which are hydrophilic ($\theta = 30°$). Given though that lately there is increased interest in the use of hydrophobic surfaces and water is widely used in many microfluidic applications, here we have decided to examine the case of a trench with $\theta = 90°$ in more detail. Thus, we performed a series of simulations and produced the flow map that appears in Fig. 19. Clearly, this map demonstrates that the coating behavior of water is poor even for relatively shallow and long trenches. It is also interesting that despite the huge difference in the liquid viscosity (and thus large difference in *Re*) the flow map in Fig. 19 exhibits many resemblances with the one in Fig. 14b. This is a clear indication that the run out length depends strongly on the wettability of the substrate affecting greatly the wetting of the upstream wall and thus the resulting coating pattern, but weakly on fluid viscosity. A directly related problem, where the surface wettability was shown to play an important role in the separation of the liquid from the solid, is the well-known "teapot effect" (Kistler and Scriven 1994). As it was shown by Duez et al. (2010) and Dong et al. (2015), this effect can be even entirely suppressed in the presence of hydrophobic surfaces.

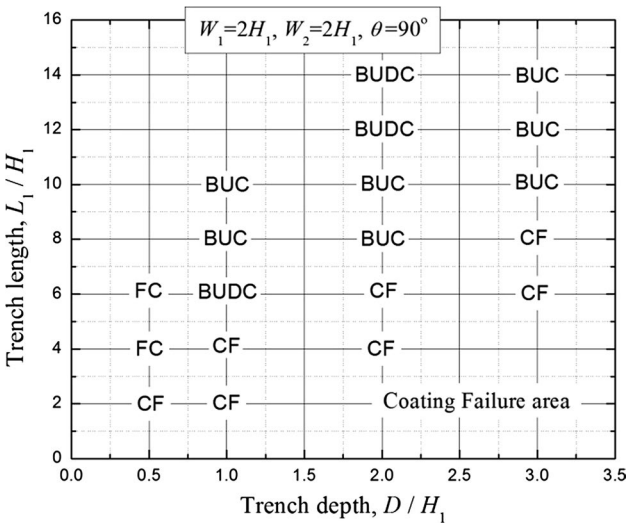

Fig. 19 (Case VII) Flow maps with possible liquid arrangements depending on D and L_1 for the case of water and a hydrophobic substrate ($\theta = 90°$). The remaining parameters are $W_1 = W_2 = 2H_1$

4.5 Multiple trenches

So far, we have examined cases where the falling liquid film wets a single trench, or more precisely, since we apply periodic boundary conditions along the sidewalls, a single periodic array of trenches. In many realistic applications, though, the coating film encounters multiple successive topographical features and one question that arises is how the coating may be affected by one trench to the next and possibly by the distance between them. To the best of our knowledge, the only study that has addressed this problem is the work presented recently by Mazloomi and Moosavi (2013). These authors employed the Lattice–Boltzmann method and studied the wetting of two successive wedges or trenches, assuming, however, that the displaced liquid has the same density and viscosity with the flowing liquid film. Their simulations have shown that the presence of a topographical feature such as a trench makes successful

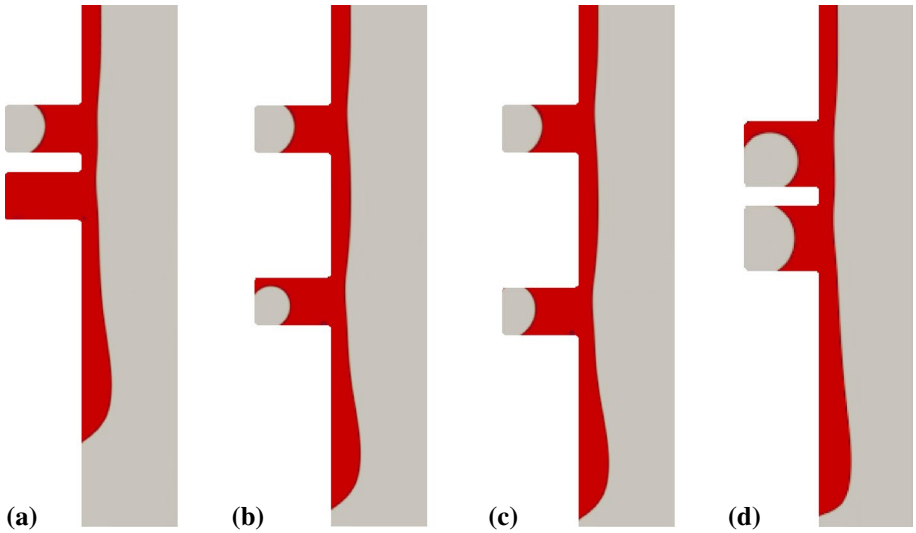

Fig. 20 (Case I) **a**–**c** Coating arrangements for two ideal 2D trenches ($D = 4H_1$ and $L_1 = 2.5H_1$) at different distances, L_5, from each other: **a** $L_5 = H_1$, **b** $L_5 = 6.5H_1$ and **c** $L_5 = 7H_1$. **d** Coating arrangements for two ideal 2D trenches ($D = 4H_1$ and $L_1 = 3.5H_1$) assuming that the gas phase has the same density and viscosity with the liquid film for $L_5 = H_1$

coating of the subsequent trench more difficult, suggesting that the required conditions for coating of the substrates with many topographical features may differ from the case of a substrate with a single topographical feature.

It is important to note though that the system that was examined by Mazloomi and Moosavi (2013) differs qualitatively from ours, since we examine the case of a liquid film that displaces air, and therefore, the density and viscosity between the two liquids differ significantly. To examine how the coating is affected in our case, we have performed simulations considering first the case of two successive ideal 2D trenches; such a configuration has not been examined by Lampropoulos et al. (2016). Our simulations, however, indicate that for a liquid–gas system the first trench actually helps the successful coating of the subsequent trench, which is exactly the opposite behavior than the one described by Mazloomi and Moosavi (2013). More specifically, we found that for cases where the first trench is partially coated, the second trench may be successfully coated, whereas for cases that the first trench was fully coated (even for the ones in the limiting regimes) we always found that the second trench was also fully coated.

A characteristic example is presented in Fig. 20a–c where we depict the resulting coating for two identical trenches with depth $D = 4H_1$ and length $L_1 = 2.5H_1$ at three different distances, L_5, from each other. Under these conditions, the first trench is only partially coated (capping failure); this is in line with the predictions of Lampropoulos et al. (2016) for a single trench with same dimensions. The coating arrangement of the second trench, however, depends on the distance between the two trenches. When this distance is small (see Fig. 20a), the second trench becomes fully wetted. On the other hand, increasing the distance between the trenches we find that the coating configurations turns from BDC for $L_5 = 6.5H_1$ to CF for $L_5 = 7H_1$ (see Fig. 20b, c); for even larger distances, we find that coating becomes identical for both trenches. This behavior can be explained as follows. In Fig. 20a, because of the small distance between the trenches, the ridge does not have enough time to recover its shape and velocity; the latter decreases as the liquid fills the first trench. The deceleration of the film leads to an enhancement of the effect of capillary forces which drive more effectively liquid inside the second trench thus resulting in successful wetting. With increasing distance between the trenches, the liquid film approaches its fully developed shape and the resulting coating approaches the behavior predicted for a single trench. In order to find out whether the different behavior between our simulations and the ones presented by Mazloomi and Moosavi (2013) is due to the effect of the density and viscosity of the displaced phase, we have also performed simulations, assuming that the viscosity and density of the gas phase are the same with the liquid (see Fig. 20d). Indeed, in this case, we found that the entrapped bubble in the second trench becomes larger which is in line with the predictions presented by Mazloomi and Moosavi (2013). This clearly suggests that the properties of the second phase do play a significant role, and therefore, these systems are not at all similar. The different behavior in the case presented in Fig. 20d can be actually attributed to the fact that the liquid film encounters increased viscous resistance from the second fluid inside the trench, thus making it more difficult to displace it in order to coat the substrate.

Finally, we turn our attention back to the case of three-dimensional topographical features and examine the case of two successive trenches. Such a simulation is presented in Fig. 21 where we examine the case of two identical trenches with $D = W_1 = 4H_1$, $L_1 = 2.5H_1$ and $W_2 = 2H_1$ at a distance $L_5 = H_1$. To our surprise, despite the very small distance between the trenches, we found that the differences in

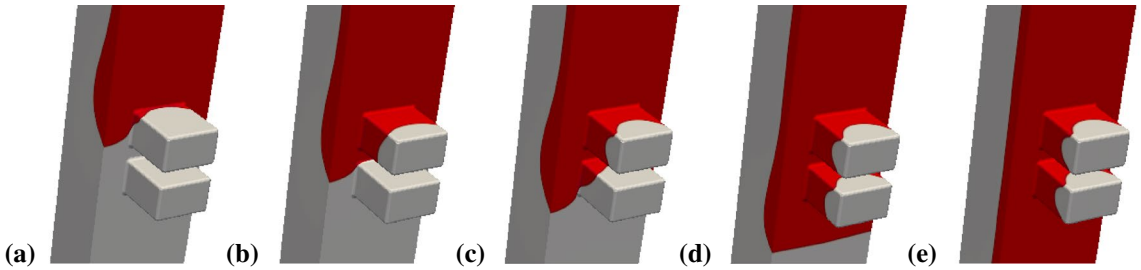

Fig. 21 (Case I) Development of a liquid film partially filling two trenches. The remaining parameters are $D = 4H_1$, $L_1 = 2.5H_1$, $W_1 = 4H_1$, $W_2 = 2H_1$, $L_5 = H_1$ and $\theta = 30°$. The corresponding times are **a** $t = 3.89$, **b** $t = 8.09$, **c** $t = 12.29$, **d** $t = 16.49$ and **e** $t = 29.09$

the coating of both trenches are insignificant. Besides this specific case, we have also examined a range of different cases (e.g., different widths of trench and lateral distance between trenches) and the differences were always found to be rather small. A significant difference between the ideal 2D case and the 3D case is that in the former all the liquid has to pass through the trench whereas in the latter part of the liquid continues its course along the flat part of the substrate next to the trench which helps the liquid recover much sooner as it exits the trench. It appears, therefore, that due to the three-dimensional character of the flow the effect of the distance between two successive trenches becomes less important on the resulting coating configuration. The latter can be considered as rather comforting since it allows us to draw more general conclusions regarding the resulting coating arrangement of realistic surfaces even by just looking the simplistic case like the coating of a single trench.

5 Conclusions

We have investigated the time-dependent flow of a gravity-driven viscous film over three-dimensional rectangular cuboid trenches. For the purposes of this study, we fully accounted for the flow in both the liquid and gas phases by solving the Navier–Stokes equations using the VOF method. The code that we have developed was implemented using the open source "OpenFOAM" software. We performed an extended parametric study to determine the different wetting patterns that may arise depending on parameters such as the various geometrical characteristics of the trench, the lateral distance between them, the substrate wettability and the liquid viscosity.

We presented flow maps which describe under which conditions the liquid film may successfully coat the patterned substrate without the presence of air inclusions; this is highly desired, e.g., in the coating of various microelectronic applications. In general, our results indicate that the full coating of a 3D trench becomes more difficult than for ideal 2D trenches, i.e., trenches with infinite width. This is mainly due to the presence of the sidewalls which are responsible for the increased viscous resistance that the liquid encounters making it more difficult to penetrate the trench. For very narrow trenches, the effect of capillarity also comes into play; its role, however, is mixed since it strongly depends on the wettability of the material. For hydrophilic surfaces, capillarity enhances coating by increasing considerably the run out length, while the opposite behavior should be expected in the case of hydrophobic surfaces. In line with common experience, it is also found that with decreasing hydrophilicity of the material the size of the entrapped air inside the topography increases considerably and in some cases may even approach the ideal Cassie–Baxter state. Examination of the coating behavior for a wide range of liquids and for mildly hydrophilic surfaces also revealed that partial coating is favored for liquids with high and low viscosities whereas liquids with moderate viscosity may favor successful coating of the patterned surface. The coating of multiple successive trenches has also been examined for both ideal 2D trenches and 3D trenches. In the former case, it was shown that when the distance between two successive trenches is small, the first trench assists the successful coating of the subsequent trench. However, it is shown that in case of 3D trenches this effect becomes much less significant. This is an important finding since these results imply that by just looking the simplistic case of the coating of a single trench it is possible to draw more general conclusions regarding the resulting coating arrangement of realistic surfaces, significantly reducing the computational cost.

The present theoretical analysis was focused on the dynamics and kinematics of the flow and the conditions that may lead to air entrapment inside the topographical features of the solid surface. It would also be interesting to examine in detail the case of a two-fluid system since some preliminary simulations that were briefly discussed in the final section of our paper indicate that the properties of the second phase play a significant role and could give rise to very different dynamics. Moreover, we would like to note that despite the interest by many research groups in

the flow over structured surfaces, very little attention has been paid, to the best of our knowledge, by experimentalists on how the entrapment takes place. We believe that our study should be supplemented by carefully designed experiments which would verify our findings and, perhaps, reveal other possible arrangements as well. On the theoretical side, our study leaves open the question about the stability of the final arrangement. Newtonian films flowing over the limited length of the topography have been shown to be remarkably stable (Kalliadasis and Homsy 2001) as compared to film flows over a flat wall, and one question that arises is how the presence of an additional liquid–air interface may affect the long-term stability of the film. Moreover, in many practical applications the flowing liquid can be a polymeric solution which often exhibits elastic effects. Pavlidis et al. (2016) have shown that elasticity works cooperatively with surface tension to drive liquid inside the trench which suggests that successful coating with a viscoelastic liquid could be easier, albeit this effect could be mitigated by the fact that these liquids typically exhibit high viscosities. Such efforts are under way.

Acknowledgements This work has been supported financially by the General Secretariat of Research and Technology of Greece through the program "Excellence" (Grant No. 1918, entitled "FilCoMicrA") in the framework "Education and Lifelong Learning" co-funded by the European Social Fund and National Resources (NL, YD and JT) and by the LIMMAT foundation under the grant MuSiComPS (GK). Part of the computations were performed on the "ARIS" National HPC Infrastructure of the Greek Research and Technology Network.

References

Argyriadi K, Vlachogiannis M, Bontozoglou V (2006) Experimental study of inclined film flow along periodic corrugations: the effect of wall steepness. Phys Fluids 18:012102

Belyaev AV, Vinogradova OI (2010) Effective slip in pressure-driven flow past super-hydrophobic stripes. J Fluid Mech 652:489–499

Bhushan B, Jung YC, Koch K (2009) Micro-, nano- and hierarchical structures for superhydrophobicity, self-cleaning and low adhesion. Phil Trans R Soc A 367:1631–1672

Bodji MS, Kumar SV, Asthana A, Govardhan RN (2009) Underwater sustainability of the "Cassie" state of wetting. Langmuir 25:12120–12126

Bontozoglou V, Serifi K (2008) Falling film flow along steep two-dimensional topography: the effect of inertia. Int J Multiph Flow 34:734–747

Brackbill JU, Kothe DB, Zemach C (1992) A continuum method for modeling surface-tension. J Comp Phys 100:335–354

Busse A, Sandham ND, McHale G, Newton MI (2013) Change in drag, apparent slip and ptimum air layer thickness for laminar flow over an idealized superhydrophobic surface. J Fluid Mech 727:488–508

Byun D, Kim J, Ko HS, Park HC (2008) Direct measurement of slip flows in superhydrophobic microchannels with transverse grooves. Phys Fluids 20:113601

Cotin-Bizonne C, Barrat JL, Bocquet L, Charlaix E (2003) Low-friction flows of nanopatterned interfaces. Nat Mater 2:237–240

Craster RV, Matar OK (2009) Dynamics and stability of thin liquid films. Rev Mod Phys 81:1131–1198

Davies J, Maynes D, Webb BW, Woolford B (2006) Laminar flow in a microchannel with superhydrophobic walls exhibiting transverse ribs. Phys Fluids 18:087110

Decré MMJ, Baret JC (2003) Gravity-driven flows of viscous liquids over two-dimensional topographies. J Fluid Mech 487:147–166

Dilip D, Bodji MS, Govardhan RN (2015) Effect of absolute pressure on flow through a textured hydrophobic microchannel. Microfluid Nanofluid 19:1409–1427

Dong Z, Wu L, Li N, Ma J, Jlang L (2015) Manipulating overflow separation directions by wettability boundary positions. ACS Nano 9:6595–6602

Duez C, Ybert C, Clanet C, Bocquet L (2010) Wetting controls separation of inertial flows from solid surfaces. Phys Rev Lett 104:084503

Fraggedakis D, Kouris Ch, Dimakopoulos Y, Tsamopoulos J (2015) Flow of two immiscible fluids in a periodically constricted tube: transitions to stratified, segmented, Churn, spray or segregated flow. Phys Fluids 27:082102

Gao P, Feng JJ (2009) Enhanced slip on a patterned substrate due to depinning of the contact line. Phys Fluids 21:102102

Gaskell PH, Jimack PK, Sellier M, Thompson HM, Wilson CT (2004) Gravity-driven flow of continuous thin liquid films on non-porous substrates with topography. J Fluid Mech 509:253–280

Goodwin R, Homsy GM (1991) Viscous flow down a slope in the vicinity of a contact line. Phys Fluids A 3(4):515–528

Gopala VR, van Wachem B (2008) Volume of fluid for immiscible-fluid and free-surface flows. Chem Eng J 141:204–221

Gramlich CM, Mazouchi A, Homsy GM (2004) Time-dependent free surface Stokes flow with a moving contact line. II. Flow over wedges and trenches. Phys Fluids 16:1660–1667

Grau G, Cen J, Kang H, Kitsomboonloha R, Scheideler WJ, Subramanian V (2016) Gravure-printed electronics: recent progress in tooling development, understanding of printing physics, and realization of printed devices. Flex Print Electron 1:023002

Hayes M, O'Brien SBG, Lammers JH (2000) Green, function for steady flow over a small two-dimensional topography. Phys Fluids 12:2845

Heining C, Aksel N (2009) Bottom reconstruction in thin-film flow over topography: steady solution and linear stability. Phys Fluids 21:083605

Higuera FJ, Medina A, Linan A (2008) Capillary rise of a liquid between two vertical plates making a small angle. Phys Fluids 20:102102

Huang C, Wang Z (2014) Planarization of high topography surfaces with deep holes and cavities using two-step polymer coating. Sens Actuators A 213:94–101

Huppert HE (1982) Flow and instability of a viscous current down a slope. Nature 300:427–429

Kalliadasis S, Bielarz C, Homsy GM (2000) Steady free surface thin film flows over topography. Phys Fluids 12:1889

Kalliadasis S, Homsy GM (2001) Stability of free-surfcae thin film flows over topography. J Fluid Mech 448:387–410

Karapetsas G, Chamakos NT, Papathanasiou AG (2016) Efficient modelling of droplet dynamics on complex surfaces. J Phys Condens Matter 28:085101

Kistler SF, Scriven LE (1994) The teapot effect: sheet-forming flows with deflection, wetting and hysteresis. J Fluid Mech 263:19–62

Kondic L, Diez J (2001) Pattern formation in the flow of thin films down an incline: constant flux configuration. Phys Fluids 13:3168

Lampropoulos NK, Dimakopoulos Y, Tsamopoulos J (2016) Transient flow of gravity-driven viscous films over substrates with rectangular topographical features. Microfluid Nanofluid 20:51

Lenz RD, Kumar S (2007) Steady two-layer flow in a topographically patterned channel. Phys Fluids 19:102103

Lv P, Xue Y, Shi Y, Lin H, Duan H (2014) Metastable states and wetting transition of submerged superhydrophobic structures. Phys Rev Lett 112:196101

Maynes D, Jeffs K, Woolford B, Webb BW (2007) Laminar flow in a microchannel with hydrophobic surface patterned microribs oriented parallel to the flow direction. Phys Fluids 19:093603

Mazloomi A, Moosavi A (2013) Thin liquid film flow over substrates with two topographical features. Phys Rev E 87:022409

Mazouchi A, Homsy GM (2001) Free surface Stokes flow over topography. Phys Fluids 13(10):2751–2761

Mazouchi A, Gramlich CM, Homsy GM (2004) Time-dependent free surface Stokes flow with a moving contact line. I. Flow over plane surfaces. Phys Fluids 16(5):1647–1659

Ou J, Rothstein JP (2005) Direct velocity measurements of the flow past drag-reducing ultrahydrophobic surfaces. Phys Fluids 17:103606

Park H, Park H, Kim J (2013) A numerical study of the effects of superhydrophobic surface on skin-friction drag in turbulent channel flow. Phys Fluids 25(11):110815

Pavlidis M, Dimakopoulos Y, Tsamopoulos J (2010) Steady viscoelastic film flow over 2D topography: I. The effect of viscoelastic properties under creeping flow. J Non Newt Fluid Mech 165:576–591

Pavlidis M, Karapetsas G, Dimakopoulos Y, Tsamopoulos J (2016) Steady viscoelastic film flow over 2D topography: II. The effect of capillarity, inertia and substrate geometry. J Non Newt Fluid Mech 234:201–214

Ponomarenko A, Quére D, Clanet C (2011) A universal law for capillary rise in corners. J Fluid Mech 666:146–154

Quére D (2005) Non-sticking drops. Rep Prog Phys 68:2495–2532

Rawlings C, Wolf H, Hedrick JL, Coady DJ, Duerig U, Knoll AW (2015) Accurate location and manipulation of nanoscaled objects buried under spin-coated films. ACS Nano 9:6188–6195

Rothstein JP (2010) Slip on superhydrophobic surfaces. Annu Rev Fluid Mech 42:89–109

Spaid MA, Homsy GM (1996) Stability of Newtonian and viscoelastic dynamic contact lines. Phys Fluids 8:460–478

Stillwagon LE, Larson RG (1990) Leveling of thin films over uneven substrates during spin coating. Phys Fluids 2:1937–1944

Teo CJ, Khoo BC (2010) Flow past superhydrophobic surfaces containing longitudinal grooves: effects of interface curvature. Microfluid Nanofluid 9:499–511

Troian SM, Herbolzheimer E, Safran SA, Joanny JF (1989) Fingering instabilities of driven spreading films. Europhys Lett 10:25–30

Tsai P, Peters AM, Pirat C, Wessling M, Lammertink RGH, Lohse D (2009) Quantifying effective slip length over micropatterned hydrophobic surfaces. Phys Fluids 21(11):112002

Veremieiev S, Thompson HM, Gaskell PH (2015) Free-surface film flow over topography: full three-dimensional finite element solutions. Comp Fluids 122:66–82

Wardle KE, Weller HG (2013) Hybrid Multiphase CFD solver for coupled dispersed/segregated flows in liquid–liquid extraction. Int J Chem Eng 2013:1–13

Xiang Y, Xue Y, Lv P, Li D, Duan H (2016) Influence of fluid flow on the stability and wetting transitions of submerged superhydrophobic surfaces. Soft Matter 12:4241–4246

Yin X, Kumar S (2006) Flow visualization of the liquid-emptying process in scaled-up gravure grooves and cells. Chem Eng Sci 61:1146–1156

Zhou C, Kumar S (2012) Two-dimensional two-layer channel flow near a step. Chem Eng Sci 81:38–45